

Supplementary Information

Àlex Solé^{a,b}, Albert Mosella-Montoro^a, Joan Cardona^b, Silvia Gómez-Coca^{*b},
Daniel Aravena^{*c}, Eliseo Ruiz^{*b} and Javier Ruiz-Hidalgo^{*a}

^a Image Processing Group - Signal Theory and Communications
Department, Universitat Politècnica de Catalunya, Barcelona, Spain;
E-mail: j.ruiz@upc.edu

^b Inorganic and Organic Chemistry Department and Institute of
Theoretical and Computational Chemistry, Universitat de Barcelona,
Barcelona, Spain; E-mail: silvia.gomez@qi.ub.es,
eliseo.ruiz@qi.ub.edu

^c Materials Chemistry Department, Faculty of Chemistry and Biology,
Universidad de Santiago de Chile, Santiago, Chile. E-mail:
daniel.aravena.p@usach.cl

S1 Envelope

Figure S1 shows the Envelope function compared with the histogram of the number of edges in the test set from the ADP dataset. The histogram is consistent with the distribution of interatomic distances described by previous works¹. Showing covalent peaks with multiple hits at short distances, and also a large number of long-distance peaks related to contacts. Further confirming that weaker intermolecular interactions play a significant role in our dataset.

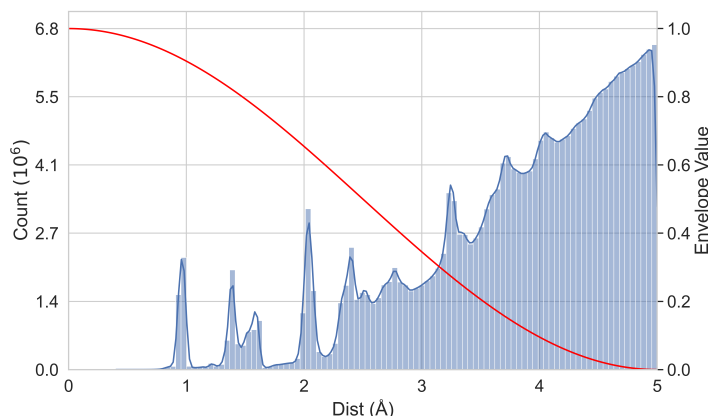


Figure S1 Histogram illustrating the distribution of edges in the test split of the ADP dataset. In blue, the distribution of the number of edges (displayed on the left y-axis) as a function of the distance between atoms in Å. The red curve represents the Envelope over distance, plotted on the right y-axis.

S2 Rotation SO(3) ADP

Given \mathbf{U}_i as the covariance matrix of atom i , \mathbf{U}_i can be decomposed using the expected value of a set of N random samples, as defined in Equation (1).

$$\mathbf{U}_i = \mathbb{E}(\mathbf{X}\mathbf{X}^T) - \mathbb{E}(\mathbf{X})\mathbb{E}(\mathbf{X}^T) \in \mathbb{R}^{3 \times 3} \quad (1)$$

Where \mathbf{X} is a matrix with the coordinates of the N random samples, such that $\mathbf{X} \in \mathbb{R}^{N \times 3}$. The rotated version of \mathbf{X} is given by $\mathbf{X}' = \mathbf{R}\mathbf{X}$. The rotated covariance matrix, therefore, can be derived as Equation (2).

$$\begin{aligned}
\mathbf{U}_i^{\text{aug}} &= \mathbb{E}(\mathbf{X}'\mathbf{X}'^T) - \mathbb{E}(\mathbf{X}')\mathbb{E}(\mathbf{X}'^T) \\
&= \mathbb{E}(\mathbf{R}\mathbf{X}\mathbf{X}^T\mathbf{R}^T) - \mathbb{E}(\mathbf{R}\mathbf{X})\mathbb{E}(\mathbf{X}^T\mathbf{R}^T) \\
&= \mathbf{R}\mathbb{E}(\mathbf{X}\mathbf{X}^T)\mathbf{R}^T - \mathbf{R}\mathbb{E}(\mathbf{X})\mathbb{E}(\mathbf{X}^T)\mathbf{R}^T \\
&= \mathbf{R}(\mathbb{E}(\mathbf{X}\mathbf{X}^T) - \mathbb{E}(\mathbf{X})\mathbb{E}(\mathbf{X}^T))\mathbf{R}^T \\
&= \mathbf{R}\mathbf{U}_i\mathbf{R}^T \in \mathbb{R}^{3 \times 3}
\end{aligned} \tag{2}$$

This derivation demonstrates how the covariance matrix \mathbf{U}_i is transformed under rotation, ensuring that the rotated ellipsoid maintains its correct orientation relative to the input data.

S3 Intersection over Union (IoU) computation

The Intersection over Union (IoU) of two ADPs is not straightforward to compute analytically. To address this, the 3D space defined by $[-1, 1]^3$ is discretized into a voxel grid with dimensions $64 \times 64 \times 64$. To ensure that both the true and predicted ellipsoids are confined within the $[-1, 1]^3$ space, the ellipsoids are normalized by the maximum norm between the true and predicted ellipsoid matrices \mathbf{U} . The Mahalanobis distance is computed for each voxel relative to the predicted and ground truth ellipsoids. The Mahalanobis distance measures the distance between a point and a distribution and is given by the Equation 3

$$D_M(\mathbf{x}) = \sqrt{\mathbf{x}^T \mathbf{U}_{\text{norm}}^{-1} \mathbf{x}} \tag{3}$$

Where \mathbf{U}_{norm} is defined as $\frac{\mathbf{U}}{\max(\|\mathbf{U}_{\text{pred}}\|, \|\mathbf{U}_{\text{true}}\|)}$, and \mathbf{x} represents the coordinates of the voxel center.

The resulting distance map is then binarized using a threshold of 1, such that voxels with $D_M(\mathbf{x}) \leq 1$ are considered inside the ellipsoid, while the rest are considered outside. The IoU is subsequently computed using the binarized distance maps for predicted and ground truth ellipsoids. Two examples of the binarized voxel grid and their respective IoU can be seen in Figure S2.

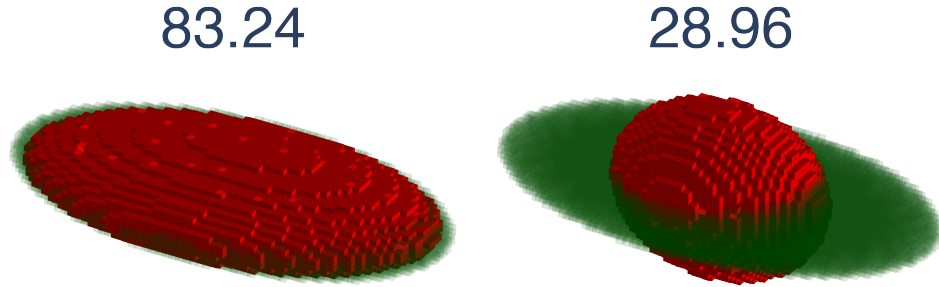


Figure S2 Visual examples of the voxelization method and the respective IoU. The green regions represent the ground truth values and the red ones the predicted. The green regions have been plotted semitransparent to facilitate the visualization of the intersection between the two regions.

S4 Training Details

In this section, we outline the specific training configurations employed for each dataset. For all the trainings, Adam² optimizer with OneCycle³ scheduler with pct start of 0.01 policy has been used. For the Jarvis and the Material Project dataset, we modified the head of the CartNet to be able to predict a scalar value (s). The prediction head, MLP_{head} , replaces the Cholesky head for these two datasets. It consists of two linear layers: the first reduces the dimensionality from dim to $\text{dim}/2$, followed by a SiLU activation function, and the second further reduces the dimensionality from $\text{dim}/2$ to 1. The

final output is obtained by applying MLP_{head} to each latent vector h_i^L and then averaging the resulting scalar values across all nodes within the unit cell, denoted by AVG . Equation (4) defines mathematically the architecture used.

$$s = AVG(MLP_{head}(h_i^L)) \quad (4)$$

Where h_i^L denote the latent vector at the final CartNet layer for atom i .

S4.1 ADP Dataset

The configuration used for training the different state-of-the art models in the ADP Dataset can be found in Table S1.

Table S1 Training configuration used for the ADP Dataset

Method	#Layers	Embedding Dim	Batch Size	Batch Accumulation	Lr	Epochs	Loss	SO(3) Augmentation	Neigh. Strategy
iComformer	4	256	4	16	$1 \cdot 10^{-3}$	50	L1	False	KNN-25
eComformer	4	256	4	16	$1 \cdot 10^{-3}$	50	L1	False	KNN-25
Ours	4	256	4	16	$1 \cdot 10^{-3}$	50	L1	True	Radius Graph (5 Å)

S4.2 Jarvis Dataset

The specific configurations used for training the different properties the Jarvis dataset provides are detailed in Table S2.

Table S2 Training configuration used for the Jarvis dataset.

Property	#Layers	Embedding Dim	Batch Size	Batch Accumulation	Lr	Epochs	Loss	SO(3) Augmentation	Neigh. Strategy
Formation Energy	4	256	64	1	$1 \cdot 10^{-3}$	500	L1	False	Radius Graph (5 Å)
Band Gap (OPT)	4	256	64	1	$1 \cdot 10^{-3}$	500	L1	False	Radius Graph (5 Å)
Total Energy	4	256	64	1	$1 \cdot 10^{-3}$	500	L1	False	Radius Graph (5 Å)
Band Gap (MBJ)	4	256	64	1	$1 \cdot 10^{-3}$	500	L1	False	Radius Graph (5 Å)
Ehull	4	256	64	1	$1 \cdot 10^{-3}$	500	L1	False	Radius Graph (5 Å)

S4.3 The Materials Project Dataset

The specific configurations used for training the different properties the Materials Project dataset provides are detailed in Table S3.

Table S3 Training configuration used for the Materials Project dataset.

Property	#Layers	Embedding Dim	Batch Size	Batch Accumulation	Lr	Epochs	Loss	SO(3) Augmentation	Neigh. Strategy
Formation Energy	4	256	64	1	$1 \cdot 10^{-3}$	500	L1	False	Radius Graph (5 Å)
Band Gap	4	256	64	1	$1 \cdot 10^{-3}$	500	L1	False	Radius Graph (5 Å)
Form. Energy	4	256	64	1	$1 \cdot 10^{-3}$	500	L1	False	Radius Graph (5 Å)
Band Gap	4	256	64	1	$1 \cdot 10^{-3}$	500	L1	False	Radius Graph (5 Å)

S5 Results Analysis

In addition we have evaluated the ADPs and the performance of our model for several chemical interactions or atom types. Table S4 summarizes these results. In addition to the MAE, S_{12} , and the IoU, we include the volume of the experimental ellipsoid that provides a reference for the typical spatial extent associated with each atom type. For comparison purposes, the metrics for all the atoms and only carbon atoms have been included as "Any" and C, respectively. For this analysis, two

typical intermolecular interactions have been considered, hydrogen bonds and π - π -interactions between benzene rings. For H-bonds the definition employed by CSD has been used and for π - π -interactions only benzene rings with centroids at a distance between 3 and 4 Å have been considered.

Table S4 Analysis of the results for different atom types of the ADP test dataset. Arrows indicate the direction of improvement for each metric.

Atom type	Volume (Å ³)	MAE (Å ²)↓	S_{12} (%)↓	IoU (%)↑
Any	$3.08 \cdot 10^{-2}$	$2.88 \cdot 10^{-3}$	0.75	83.53
C	$3.12 \cdot 10^{-2}$	$2.90 \cdot 10^{-3}$	0.74	83.70
$R = N, O, S$ in H-bond ($R-H \cdots R'$)	$2.52 \cdot 10^{-2}$	$2.65 \cdot 10^{-3}$	0.89	82.14
$R' = N, O, F, Cl, Br, I$ in H-bond ($R-H \cdots R'$)	$2.76 \cdot 10^{-2}$	$2.75 \cdot 10^{-3}$	0.83	82.78
C in $\pi - \pi$ interaction	$2.76 \cdot 10^{-2}$	$2.43 \cdot 10^{-3}$	0.66	85.54
central C in tert-Butyl	$2.23 \cdot 10^{-2}$	$2.33 \cdot 10^{-3}$	0.78	82.80
methyl C in tert-Butyl	$3.84 \cdot 10^{-2}$	$3.81 \cdot 10^{-3}$	0.73	83.60

For atoms participating in hydrogen bonds, moderate MAEs ($\sim 2.65 \times 10^{-3} \text{ Å}^2$ to $2.75 \times 10^{-3} \text{ Å}^2$) are observed, alongside slightly elevated S_{12} values (0.89 and 0.83). In these atoms the experimental volumes ($\sim 2.52 \times 10^{-2} \text{ Å}^3$ to $2.76 \times 10^{-2} \text{ Å}^3$) are smaller than all the atom types ($\sim 3.08 \times 10^{-2} \text{ Å}^3$) indicating some spatial constraints as expected, even at moderate level. Beside moderates, the IoU values around 82% confirm that the predicted ellipsoids still overlap well with the reference data.

In the case of π - π -interactions between benzene rings, it stand out with an MAE of $2.43 \times 10^{-3} \text{ Å}^2$, which is lower than that of the general carbon category ($2.90 \times 10^{-3} \text{ Å}^2$). This reduced MAE aligns with their smaller average experimental volume of $2.76 \times 10^{-2} \text{ Å}^3$, compared with $3.12 \times 10^{-2} \text{ Å}^3$ for generic carbons. In other words, the ADPs in benzene rings are smaller than in other C atom types, probably due to the ring rigidity and reduced conformational flexibility. Moreover, the IoU of 85.54% for these π - π -interacting carbons exceeds both the baseline for all atoms (83.53%) and the baseline for carbons atoms (83.70%), indicating that the model recovers the shape of their displacement ellipsoids particularly well.

Additionally, the performance of the model can be affected by substituents that are more prone to disorder due to different factors, for example, more rotational freedom. One case scenario can be the tert-butyl group, that is the one analyzed here. It has two types of C atoms, the central one that is expected to have less freedom and the methyl ones that are expected to have more flexibility and consequently larger ADPs. As expected, the central carbon in the tert-butyl group, exhibits one of the smallest experimental volumes among all carbons analyzed ($2.23 \times 10^{-2} \text{ Å}^3$). Correspondingly, it shows a lower MAE ($2.33 \times 10^{-3} \text{ Å}^2$) compared to both the “Any” and generic carbon categories. This observation supports the notion that a smaller, more spatially confined environment correlates with more accurate ADP predictions. Although the IoU for this central carbon (82.80%) is similar to that of hydrogen-bonded atoms, it remains close to the baseline levels, indicating that the model is capturing the overall shape of the anisotropic displacement despite slight nuances in the ellipsoid’s geometry. Not surprisingly, the methyl carbons in tert-butyl groups occupy a larger experimental volume ($3.84 \times 10^{-2} \text{ Å}^3$) and show a higher MAE ($3.81 \times 10^{-3} \text{ Å}^2$) than any of the listed categories. However, their IoU (83.60%) remains comparable to generic carbons, indicating that the model consistently identifies the shape of the ellipsoid, and is able to properly reproduce the increased thermal motion and conformational freedom in these methyl carbons.

Overall, these results highlight the robust predictive capability of our model across a variety of atom types and interactions. In addition, the correlation between the volume and the accuracy metrics (particularly MAE) emphasizes the influence of local structural constraints, such as planarity, rigidity, or conformational freedom, on anisotropic displacement parameters.

In order to gain more insight into how the model performs in the same compound but with different crystal structures and measured at different temperatures the results for the structures of the known ROY polymorph that were in the test dataset have been analyzed. Table S5 summarizes the performance of CartNet in predicting their ADPs. The metrics examined (MAE, S_{12} , and IoU) provide complementary insights into how faithfully the model captures thermal ellipsoid shapes and orientations.

Overall, the model demonstrates robust predictive capability for the majority of the structures, often achieving high IoU values and low S_{12} and MAE metrics. Notably, several Y polymorphs (e.g., QAXMEH22, QAXMEH23, QAXMEH58) exhibit

both high IoU scores (above 88%) and minimal shape discrepancy, suggesting that CartNet can effectively capture thermal motion when the underlying structural motifs remain consistent. However, a performance reduction is observed for certain polymorphs measured at low temperatures or within the $P\bar{1}$ space group. This trend is exemplified by QAXMEH53 (Y04, $P\bar{1}$ at 100 K) and QAXMEH56 (R, $P\bar{1}$ at 150 K), which show relatively higher S_{12} values alongside lower IoU scores. Similarly, although QAXMEH19 (Y, $P2_1/n$ at 30 K) maintains a comparatively low MAE, its IoU is notably lower than other Y polymorphs at higher temperatures, indicating that temperature-induced lattice distortions or pronounced packing differences can pose additional challenges for the model.

Table S5 Table of results between the different ROY structures present in the ADP test dataset. Arrows indicate the direction of improvement for each metric.

CSD Refcode	Polymorph	Space Group	Temperature (K)	MAE (\AA^2)↓	S_{12} (%)↓	IoU (%)↑
QAXMEH32	ON	$P2_1/c$	100	$1.21 \cdot 10^{-3}$	0.56	80.95
QAXMEH54	ON	$P2_1/c$	150	$2.09 \cdot 10^{-3}$	0.44	84.44
QAXMEH55	ORP	Pbca	150	$1.74 \cdot 10^{-3}$	0.29	88.50
QAXMEH56	R	$P\bar{1}$	150	$3.98 \cdot 10^{-3}$	1.71	68.46
QAXMEH19	Y	$P2_1/n$	30	$1.26 \cdot 10^{-3}$	1.22	72.89
QAXMEH22	Y	$P2_1/n$	293	$2.56 \cdot 10^{-3}$	0.23	90.09
QAXMEH23	Y	$P2_1/n$	293	$2.50 \cdot 10^{-3}$	0.27	88.56
QAXMEH58	Y	$P2_1/n$	150	$1.31 \cdot 10^{-3}$	0.20	91.95
QAXMEH53	Y04	$P\bar{1}$	100	$2.75 \cdot 10^{-3}$	1.42	68.74
QAXMEH12	YT04	$P2_1/n$	296	$2.14 \cdot 10^{-3}$	0.16	90.93

Low temperatures were anticipated to yield less accurate ADPs, as discussed in Section 5.2.3 of the main manuscript. Nonetheless, we also examined whether there is a correlation between the IoU metric and the space groups listed in Table S5. To this end, Table S6 presents the number of structures in the ADP test dataset alongside the mean IoU value for each space group. No correlation was observed between the space groups and the IoU metric.

Table S6 Summary of space groups, number of structures, and mean IoU percentages of the ADP test dataset. Arrows indicate the direction of improvement for each metric.

Space Group	Number of Structures	IoU (%)↑
$P2_1/c$	5327	84.29
P-1	4247	84.15
$P2_1/n$	4125	83.89
Pbca	1079	83.97

S6 DFT calculations

Density functional theory (DFT) calculations were carried out employing the Vienna ab initio Simulation package (VASP v6.4.3⁴⁻⁶). ADPs were calculated based on numerical displacements around the optimized geometry, generated using the Phonopy program^{7,8} (v2.19.1). All DFT calculations were based on the PBE⁹ functional, the projector-augmented wave method ($E_{cut} = 500$ eV) and included D3-BJ¹⁰ dispersion corrections. Electron wave functions were converged to a threshold of 10^{-8} eV. Calculations were repeated for three different optimized geometries: (i) a fully relaxed structure, including atomic positions and unit cell parameters, (ii) a geometry where the unit cell was fixed to the crystallographic parameters, allowing the atomic positions to relax and (iii) a structural relaxation constrained to a fixed volume (241.23687\AA^3), calculated by the Vinet equation of state for a series of compressed and expanded unit cells using the quasi-harmonic approximation. The thermal expansion was calculated for 298K to match the experimental data from the CSD database for the ETIDEQ refcode. Structural relaxation runs considered a k-point grid of $5 \times 3 \times 2$ while the displaced geometries were calculated at the Γ point using a $5 \times 3 \times 2$ supercell. ADPs were obtained using a q-point grid of $64 \times 64 \times 64$. Regarding the computational requirements, calculations for each displaced geometry took ca. 20,000 s (5.8 hrs) to complete using 56 cores in a parallel run. The fully relaxed calculation and the one derived from the Vinet equation required 144 displace-

ments to complete while the simulations based on the experimental unit cell demanded 72 displacements, as it retained inversion symmetry. Six additional calculations, each including 144 displacements, were done for the compressed and expanded units cells.

S7 Temperature Ablation

The temperature ablations from the paper mention a series of crystal structures of *guanidinium pyridiniumnaphthalene-1,5-disulfonate*. They are used to assess the ability of CartNet to predict ADPs at other temperatures using as input the crystal structure geometry obtained at a different temperature. The refcodes used for the study with the respective temperature can be found in Table S7.

Table S7 The refcodes and the temperatures used for the temperature ablation study.

Refcode	Temperature (K)
DOWVOC28	153
DOWVOC31	163
DOWVOC33	178
DOWVOC34	183
DOWVOC36	193
DOWVOC38	203
DOWVOC40	213
DOWVOC42	223
DOWVOC44	233
DOWVOC46	243
DOWVOC48	253
DOWVOC02	263
DOWVOC04	273
DOWVOC29	283

We repeated the fixed-geometry experiment at 153 K and 283 K , adjusting only the input temperature to CartNet. Figure S3 shows results obtained with the 153 K geometry, and Figure S4 presents those from the 283 K geometry. In both cases, deviations from experimental values grow as the input temperature moves further from the reference structure. This finding indicates that significant structural rearrangements (e.g., intermolecular interactions, phase transitions) cannot be fully captured when the geometry is constant. Although CartNet accounts for some thermal expansion through temperature input, it does not accommodate large-scale reorganizations without an updated geometry. Overall, CartNet reasonably reproduces thermal ellipsoids but shows limitations when temperature changes are substantial enough to trigger phase transitions or significant structural differences.

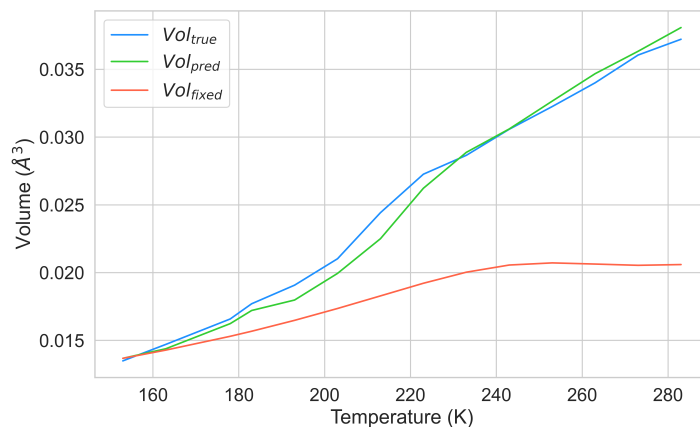


Figure S3 Comparison of mean volume of the ellipsoids as a function of temperature for the *guanidinium pyridinium naphthalene-1,5-disulfonate* (CSD refcode: DOWVOC) crystal structure. Blue line represent the experimental volumes, green line represent the predicted volume of the ellipsoid using the geometry and temperature from experimental data, and orange line represent the predicted volume of the ellipsoid when using the fixed geometry from the crystal structure at 153K and modifying the input temperature to CartNet.

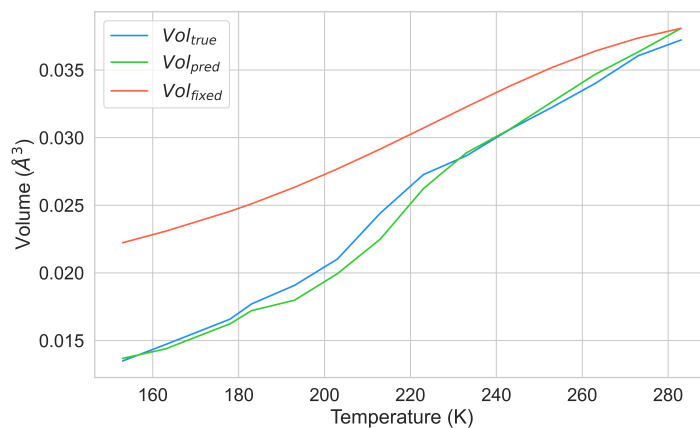


Figure S4 Comparison of mean volume of the ellipsoids as a function of temperature for the *guanidinium pyridinium naphthalene-1,5-disulfonate* (CSD refcode: DOWVOC) crystal structure. Blue line represent the experimental volumes, green line represent the predicted volume of the ellipsoid using the geometry and temperature from experimental data, and orange line represent the predicted volume of the ellipsoid when using the fixed geometry from the crystal structure at 283K and modifying the input temperature to CartNet.

S8 Visual Results

This section presents some more comparison results between the ADPs prediction of eConformer, iConformer and our proposed CartNet method.

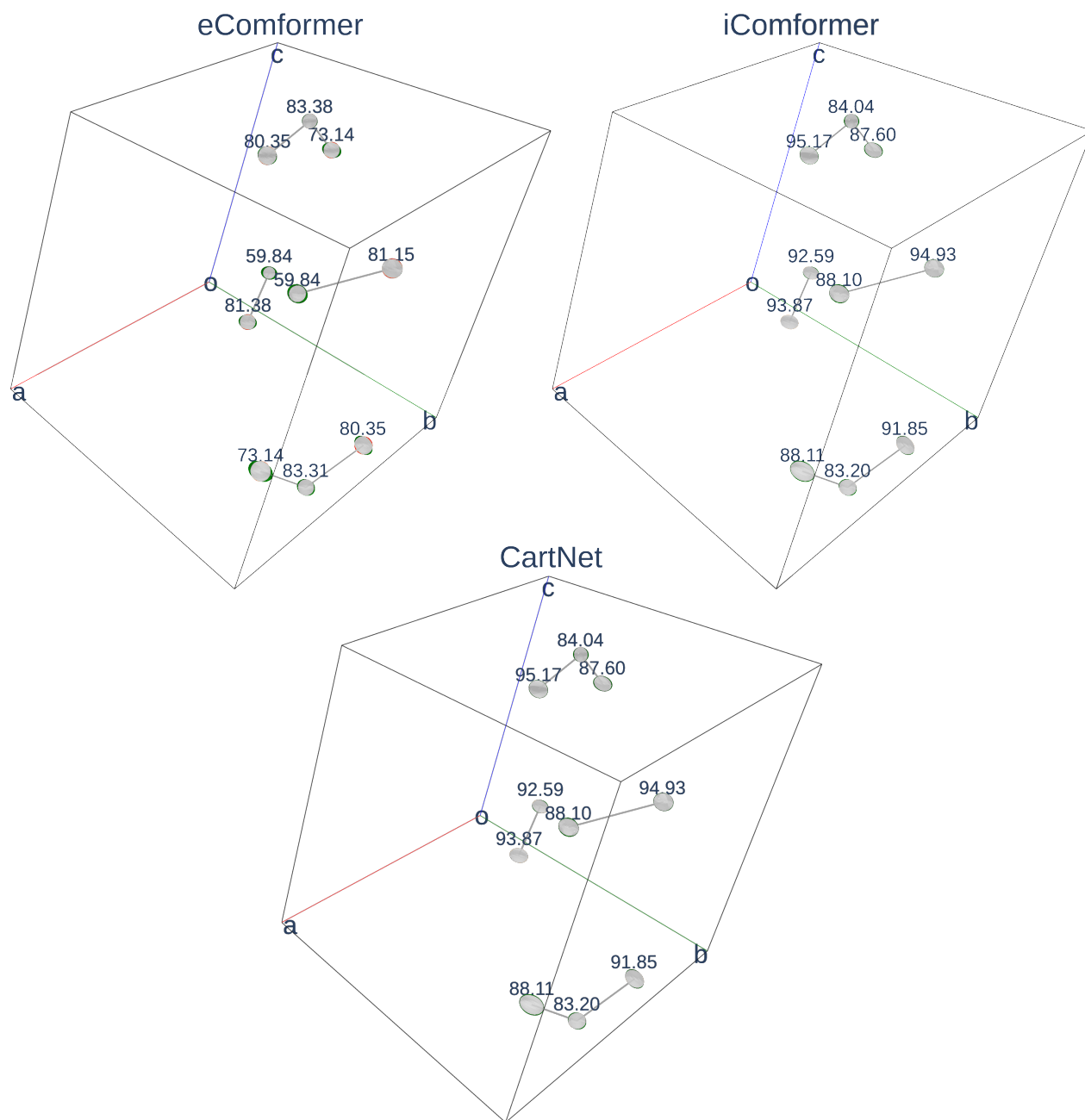


Figure S5 Thermal ellipsoids representations from experimental ADPs for the *glycine* crystal structure (CSD refcode: DOLBIR21) predicted with CartNet, eComformer and iComformer. The green regions represent the experimental values, the red ones represent the prediction values, and the grey represents the intersection between them. The numbers in each atom represent the IoU between the experimental and the calculated ADP. Highlighted can be seen a sample ellipsoid predicted using the DFT and the same ellipsoid using CartNet. The parallelepiped represents the unit cell, and the red, green, and blue lines correspond to the a, b, and c unit cell axes.

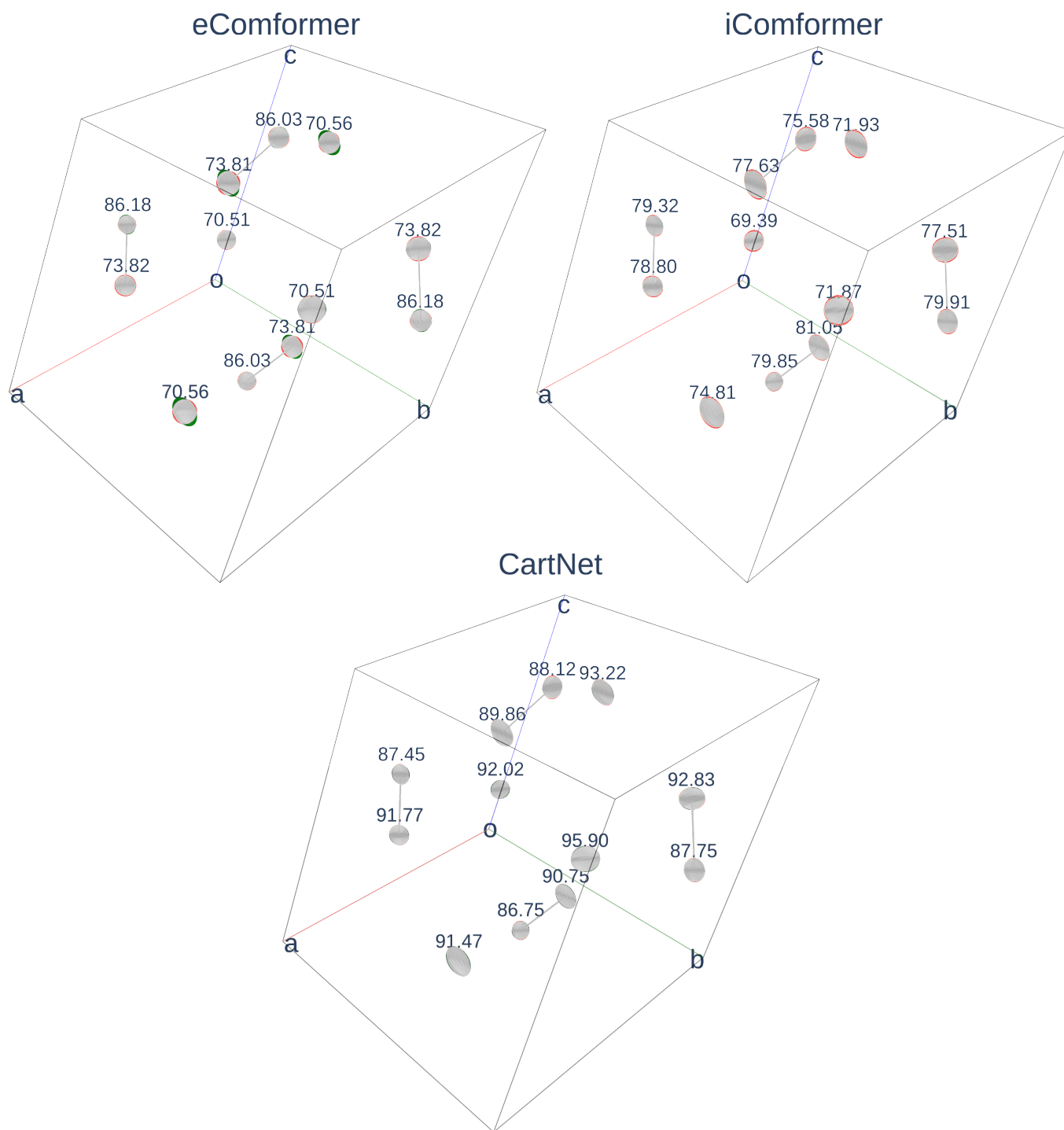


Figure S6 Thermal ellipsoids representations from experimental ADPs for the *Ethane-1,2-dioic acid* crystal structure (CSD refcode: OXALAC10) predicted with CartNet, eComformer and iComformer. The green regions represent the experimental values, the red ones represent the prediction values, and the grey represents the intersection between them. The numbers in each atom represent the IoU between the experimental and the calculated ADP. Highlighted can be seen a sample ellipsoid predicted using the DFT and the same ellipsoid using CartNet. The parallelepiped represents the unit cell, and the red, green, and blue lines correspond to the a, b, and c unit cell axes.

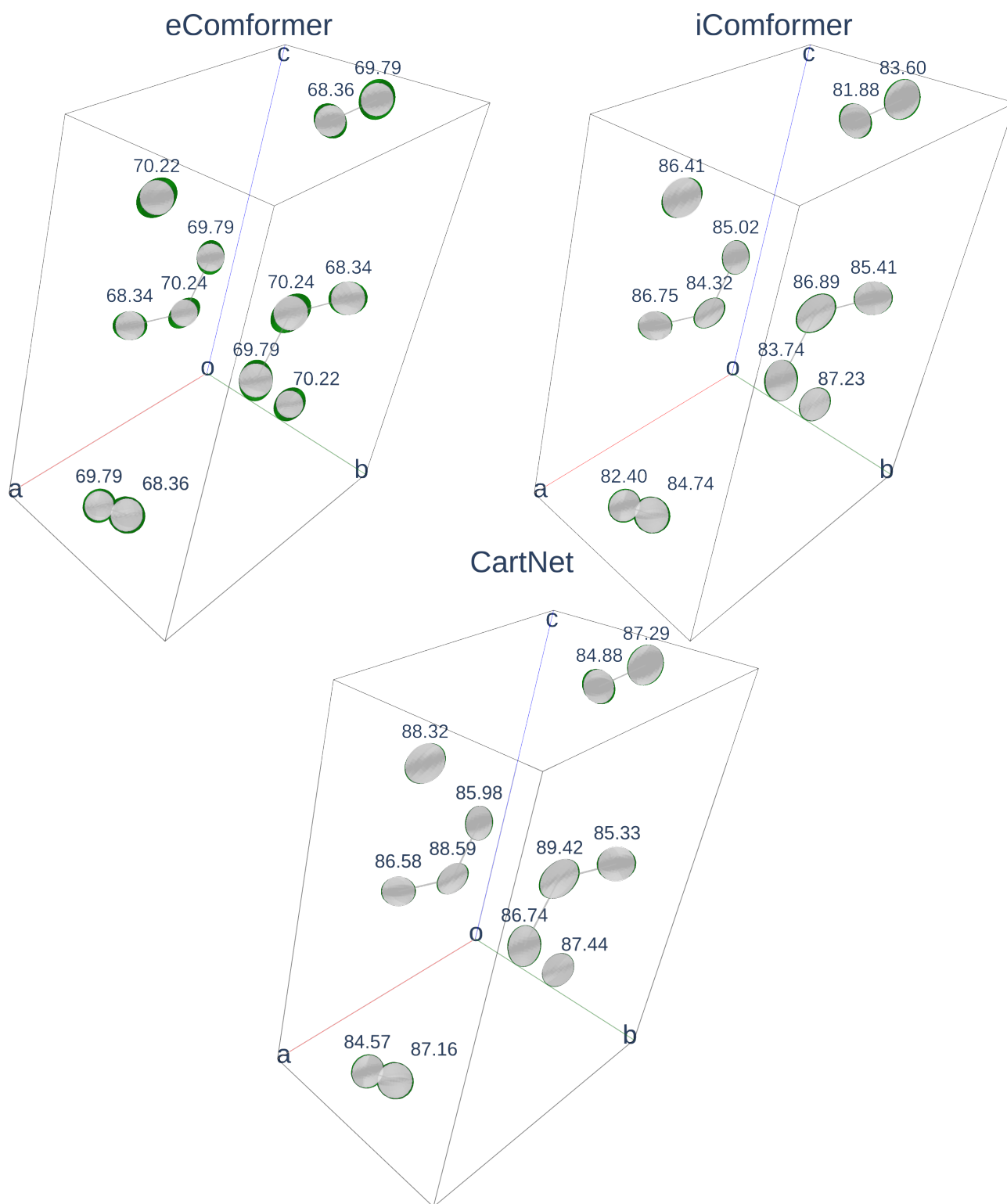


Figure S7 Thermal ellipsoids representations from experimental ADPs for the *piperazine* crystal structure (CSD refcode: ITIZOA01) predicted with CartNet, eComformer and iComformer. The green regions represent the experimental values, the red ones represent the prediction values, and the grey represents the intersection between them. The numbers in each atom represent the IoU between the experimental and the calculated ADP. Highlighted can be seen a sample ellipsoid predicted using the DFT and the same ellipsoid using CartNet. The parallelepiped represents the unit cell, and the red, green, and blue lines correspond to the a, b, and c unit cell axes.

Notes and references

- [1] S. Alvarez, *Dalton Trans.*, 2013, **42**, 8617–8636.
- [2] D. Kingma and J. Ba, International Conference on Learning Representations (ICLR), San Diego, CA, USA, 2015.
- [3] L. N. Smith and N. Topin, Artificial intelligence and machine learning for multi-domain operations applications, 2019, pp. 369–386.
- [4] G. Kresse and J. Furthmüller, *Phys. Rev. B*, 1996, **54**, 11169–11186.
- [5] G. Kresse and J. Furthmüller, *Computational Materials Science*, 1996, **6**, 15–50.
- [6] G. Kresse and J. Hafner, *Phys. Rev. B*, 1993, **47**, 558–561.
- [7] A. Togo, *J. Phys. Soc. Jpn.*, 2023, **92**, 012001.
- [8] A. Togo, L. Chaput, T. Tadano and I. Tanaka, *J. Phys. Condens. Matter*, 2023, **35**, 353001.
- [9] J. P. Perdew, K. Burke and M. Ernzerhof, *Phys. Rev. Lett.*, 1996, **77**, 3865–3868.
- [10] S. Grimme, S. Ehrlich and L. Goerigk, *Journal of Computational Chemistry*, 2011, **32**, 1456–1465.